Understanding the Correlation between Electrochemical Performance and Operating Mechanism of a Co-free Layered-Spinel Composite Cathode for Na-Ion Batteries

Aswathi Thottungal, Aswinsriram Sriramajeyam, Ammu Surendran, Harsha Enale, Angelina Sarapulova, Oleksandr Dolotko, Qiang Fu, Michael Knapp, Ditty Dixon,* and Aiswarya Bhaskar*

ABSTRACT: Compositing different crystal structures of layered transition metal oxides (LTMOs) is an emerging strategy to improve the electrochemical performance of LTMOs in sodium-ion batteries. Herein, a cobalt-free P2/P3-layered spinel composite, P2/P3-LS-$Na_{1/2}Mn_{2/3}Ni_{1/6}Fe_{1/6}O_2$ (LS-NMNF), is synthesized, and the synergistic effects from the P2/P3 and spinel phases were investigated. The material delivers an initial discharge capacity of 143 mAh g^{-1} in the voltage range of 1.5−4.0 V and displays a capacity retention of 73% at the 50th cycle. The material shows a discharge capacity of 72 mAh g^{-1} at 5C. This superior rate performance by the material could be by virtue of the increased electronic conductivity contribution of the incorporated spinel phase. The charge compensation mechanism of the material is investigated by *in operando* X-ray absorption spectroscopy (in a voltage range of 1.5−4.5 V vs Na^+/Na), which revealed the contribution of all transition metals toward the generated capacity. The crystal structure evolution of each phase during electrochemical cycling was analyzed by *in operando* X-ray diffraction. Unlike in the case of many reported P2/P3 composite cathode materials and spinel-incorporated cobalt-containing P2/P3 composites, the formation of a P′2 phase at the end of discharge is absent here.

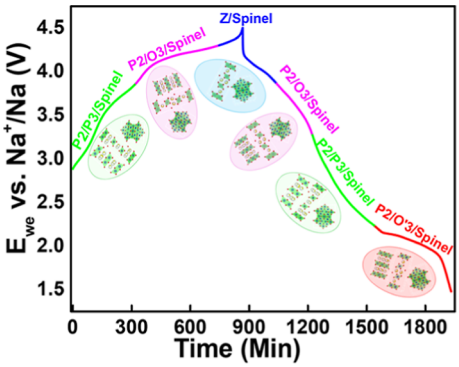

KEYWORDS: *sodium-ion batteries, cobalt-free, cathodes, layered-spinel composites, In operando X-ray absorption spectroscopy, In operando X-ray diffraction, phase transformations*

INTRODUCTION

Fossil fuel depletion, global warming, and increasing global energy demand necessitated the development of renewable energy sources like wind and solar.[1] However, the intermittent nature of renewable energy needs an efficient large-scale energy storage system.[2] Currently, lithium-ion battery (LIB) technology is ruling the rechargeable battery domain, especially in the consumable electronic as well as electric vehicle market, due to its high energy density, lack of memory effect, low self-discharge rate, and moderate power density.[3] Nevertheless, the limited abundance (≤0.002 wt %) and uneven distribution of lithium in the earth's crust make the LIB expensive and restrict its dependency on future generations. In this context, sodium-ion batteries (SIBs) are getting more attention due to their comparable electrochemical mechanism with LIB, higher natural abundance, and even distribution of Na in the earth's crust (2.36 wt %).[4]

The positive electrode (cathode) materials for SIBs, which are the capacity-limiting electrodes, are primarily classified into four: layered transition metal oxides (LTMOs), polyanionic compounds, Prussian blue analogues, and organic materials.[5] Among these, LTMOs obtained more recognition owing to their higher specific capacity, relatively simple synthesis procedures, higher ionic conductivity, and environmental compatibility.[6−8] Delmas and co-workers classified the LTMOs into P2, P3, and O3 according to their crystal structure. The letters P and O indicate the trigonal prismatic and octahedral symmetry for the sodium occupying sites, respectively, and the numbers 2 and 3 correspond to the number of oxide stacking sequences. The P2-type materials possess oxygen layer stacking sequence ABBA, whereas in O3- and P3-type materials, the stacking sequence is ABCABC and ABBCCA, respectively.[9] Even though the O-type materials contain higher sodium content, the energy barrier for Na^+ diffusion is higher compared to P-type materials as a consequence of the diffusion of sodium ions between the two octahedral sites via edge-sharing tetrahedral sites.[10−12]

Between P and O-type materials, P-type material shows superior rate capability compared to O-type on account of the easy Na^+ diffusion through two face-sharing trigonal prisms.[13−17] Even though the sodium ions in trigonal prismatic sites are stable; at higher voltages (≥4.20 V vs Na^+/Na), over extraction of sodium ions from the P2 structure brings a transition metal oxide layer gliding, which leads to a P2−O2 phase transformation.[18−20] Recently, the P3-type materials received recognition due to the higher sodium content, open prismatic diffusion channels, and low-temperature synthesis.[21] P3-type materials can be synthesized by two methods; electrochemical removal of sodium from O3-type material and low-temperature annealing of the corresponding P2-phase.[21−23] However, severe phase transformation of P3-type materials during cycling because of the poor symmetric crystal structure of the material, restricts their practical application as a high-capacity cathode material for SIBs.[21,24]

Designing a multiphase LTMO material with synergistic effects from each phase is an emerging strategy to obtain materials with superior electrochemical performance. Recently, several groups have been working on biphasic or multiphasic materials as cathode materials for SIBs.[24,25] In P2/P3 composite materials, similar crystal structures possessed by P3 and P2-type materials impart smoother sodium diffusion pathways and better structural stability during cycling.[10,26] Hence, designing a P2/P3 composite could be a better strategy to improve the electrochemical performance of LTMOs as cathodes for SIBs. Passerini et al.[49] introduced a P3/P2-composite by modulating the annealing temperature to 750 °C. The composite delivered a lower initial capacity due to the increased particle size as a result of the higher annealing temperature. However, the material exhibited better cycling stability.[26] Zhou et al. synthesized a P2/P3-composite material, P2/P3−$Na_{0.66}Co_{0.5}Mn_{0.5}O_2$, which delivered a discharge capacity of 156 mAh g^{-1} at 1C (1C = 170 mA g^{-1}) in the voltage range of 1.5−4.3 V vs Na^+/Na and exhibited 91% capacity retention at 10C after 100 cycles. These excellent battery performances can be attributed to the synergistic effects of the P3 and P2 phases, which provide faster sodium diffusion through open prismatic sites and better structure stability on cycling.[27] Yan et al. synthesized a P3/P2 composite $Na_{0.78}Cu_{0.27}Zn_{0.06}Mn_{0.67}O_2$, in which the electrochemical performance was improved by the P3 intergrowth, and the protective covering of the P3 phase suppresses the moisture sensitivity of the material.[14] Guo and co-workers developed a biphasic cathode material for SIBs, P2/P3−$Na_{0.7}Li_{0.06}Mg_{0.06}Ni_{0.22}Mn_{0.67}O_2$, by optimizing the annealing temperature to 800 °C. A discharge capacity of 119 mAh g^{-1} was obtained from the material, demonstrating a notable energy density of 218 Wh kg^{-1} in a full cell with hard carbon.[28] Rahman et al. reported a composite $Na_{0.75}Co_{0.125}Cu_{0.125}Fe_{0.125}Ni_{0.125}Mn_{0.5}O_2$, which delivered an initial capacity of 90 mAh g^{-1} along with 100% capacity retention after 100 cycles at C/10. The material showed excellent long-term cycling performances like 96% capacity retention at 1C after 500 cycles and 85% capacity retention after 1000 cycles at 5C. The excellent electrochemical performance of these composite materials can be attributed to the structural stability obtained from the ordered intergrowth of the P2 and P3 phases.[29] Wang and his group reported a P3/P2 composite $Na_{0.6}Mn_{0.75}Ni_{0.25}O_2$ prepared by a coprecipitation method, which possesses high tapped density.[30] Recently, Jiang et al. synthesized a cobalt-substituted P2/P3 composite P2/P3−$Na_{0.67}Mn_{0.64}Co_{0.30}Al_{0.06}O_2$ by a dealloying-annealing strategy. The material shows outstanding electrochemical performances, as it delivered a reversible capacity of 83 mAh g^{-1} at 10C (1700 mA g^{-1}) and excellent cycling stability over 1000 cycles at 1 A g^{-1}.[26]

The integration of a spinel phase into a layered phase is a familiar strategy for high-rate cathodes for lithium-ion batteries. However, a sodium-based spinel is thermodynamically unstable due to the large size of sodium ions. Nevertheless, Manthiram et al. developed a P2-layered-spinel composite cathode material, $Na_{0.50}Ni_{1/6}Co_{1/6}Mn_{2/3}O_2$, for SIB by modulating the sodium content, in which a sodium-free transition metal oxide is the incorporated spinel phase (Space group: $Fd\bar{3}m$). They found that the integrated spinel phase enhanced the rate performance by the higher electronic conductivity of the spinel, which helps to synchronize the sodium-ion intercalation and deintercalation with electron transport. The layered-spinel composite delivered a discharge capacity of 85 mAh g^{-1} at 10C in the voltage range of 2.0−4.5 V vs Na^+/Na.[31] In 2018, Hou et al. developed a triphasic material in which the synergistic effects of phases P2, P3, and spinel were observed. This material delivered a high reversible capacity of 105 mAh g^{-1} at a C-rate of 10C. Further, a high specific capacity of 180 mAh g^{-1} and capacity retention of 87.6% after 100 cycles at C/10 between 1.5 and 4.0 V was observed for the material.[32] A year later, S-L. Chou and co-workers designed a P2/P3 integrated spinel, $Na_{0.5}Ni_{0.1}Co_{0.15}Mn_{0.65}Mg_{0.1}O_2$, as cathode material for SIBs. They used the strategy of element substitution to suppress complex phase transformations during cycling. The material exhibited a capacity of 153.8 mAh g^{-1} at C/10 in the voltage range of 1.5−4.0 V and 97.5 mAh g^{-1} at 5C.[33] Despite the superior electrochemical performance exhibited due to the composite structure, all of these P-type layered spinel composites contain cobalt. This cobalt further contributes to the total electrochemical activity. However, the high cost and toxicity of cobalt, as well as the less abundant resources, shadow the practical application of these materials. Nevertheless, to the best of our knowledge, cobalt-free P-type layered-spinel composite cathodes are not yet reported. The major challenge for the layered cathodes without cobalt is the poor electrochemical performance and unwanted phase transformations in these materials during sodium intercalation/deintercalation.[34]

The present work reports a Fe-containing cobalt-free P2/P3-spinel composite, LS-$Na_{1/2}Mn_{2/3}Ni_{1/6}Fe_{1/6}O_2$, as a cathode material for SIBs with better electrochemical performance and structural stability. The replacement of cobalt with Fe is a promising strategy for developing an environmentally compatible, inexpensive cathode material for SIBs for future generations. The material is expected to have synergistic effects from P2, P3, and spinel phases and structural stability from the Fe-substitution.[35] The material is synthesized by the citric acid-assisted sol−gel method, and the structure, morphology, and electrochemical performance of the material were analyzed. The electrochemical mechanism and structural evolution of the material were investigated using *in operando* X-ray absorption spectroscopy (XAS) and X-ray diffraction (XRD), respectively.

EXPERIMENTAL SECTION

Synthesis of P2/P3-LS-$Na_{1/2}Mn_{2/3}Ni_{1/6}Fe_{1/6}O_2$ (LS-NMNF) Material. The layered-spinel material LS-NNMF was synthesized

by the citric-acid−based sol−gel method. Stoichiometric amounts of metal acetates such as sodium acetate trihydrate, $CH_3COONa{\cdot}3H_2O$, manganese(II) acetate tetrahydrate, $(CH_3COO)_2Mn{\cdot}4H_2O$ (Strem chemicals, ≥99%), nickel(II) acetate tetrahydrate, $(CH_3COO)_2Ni{\cdot}4H_2O$ (Sigma-Aldrich, ≥99%), and iron(II) chloride tetrahydrate, $FeCl_2{\cdot}4H_2O$ (Sigma-Aldrich, ≥99%), were added to a solution of citric acid monohydrate (Alfa Aesar) dissolved in ethylene glycol (Sigma-Aldrich) in a 1:4 molar ratio and dissolved thoroughly under constant stirring. The temperature was increased to 90 °C for the complete dissolution of the metal salts. A viscous gel was obtained at 180 °C after the evaporation of excess ethylene glycol, and this gel was then precalcined at 350 °C for 5 h at a heating rate of 5 °C per minute. The obtained precursors were then annealed at 500 °C for 6 h, followed by a final annealing at 900 °C for another 12 h. After cooling to room temperature, the material was stored in an Ar-filled glove box to protect from moisture.

Thermogravimetric Analysis. Thermogravimetric (TG) analysis of the LS-NMNF sample was performed using a NETZSCH STA 449F3 thermal analyzer instrument. TG analysis was conducted on the 350 °C pre-annealed sample under air from room temperature to 1000 °C with a heating rate of 10 °C per minute.

Chemical Composition Analysis. The elemental composition of the LS-NMNF sample was analyzed by an optical emission spectrometer (iCAP 7000 Series, Thermo Scientific) with an inductively coupled plasma ion source (ICP-OES). Three portions of the sample were taken to triplicate the measurements, and the samples were digested with acid in a graphite oven. The solutions were investigated to obtain the elemental ratios of Na, Ni, Mn, and Fe in the sample.

Structural and Morphological Investigations. Structural investigation of the LS-NMNF sample was carried out using a STOE Stadi P powder diffractometer with monochromatic Mo $K_{\alpha 1}$ radiation (λ = 0.70930 Å). The XRD measurements were carried out at angles from 3 to 51° 2θ in transmission geometry at room temperature. The Rietveld refinement based on the observed diffraction data of the composite material was carried out using the WINPLOTR package, containing FullProf program.[36] The estimated standard deviations for all the refined parameters were calculated in agreement with Berar and Lelann.[37] Field emission scanning electron microscopy (FESEM) analysis was done by using a Carl Zeiss SUPRA 55VP FESEM containing a Gemini Column with an air lock system to analyze the morphology and particle size of the as-synthesized LS-NMNF sample.

The coexistence of three phases P2, P3, and spinel was further analyzed by high-resolution transmission electron microscopy (HRTEM). The images were taken by two instruments, Talos F200S (FEI) instrument with field emission gun, operated at an accelerating voltage of 200 kV and JEOL JEM-2100 electron microscope operated at 200 kV accelerating voltage with LaB_6 electron source.

X-ray Photoelectron Spectroscopy Investigations. To reveal the oxidation states of the transition metals on the surface, X-ray photoelectron spectroscopy (XPS) analysis was performed using an ESCALAB 250xi Base system with UPS and XPS image mapping and XR6 Microfocused Monochromator (Al Kα XPS), XR4 Twin Anode Mg/Al (300/400 W) X-ray Source, and EX06 Ion gun as source. The results obtained from the measurements were further analyzed by using the software CasaXPS.

Electrochemical Characterization. The electrodes of as-synthesized LS-NMNF material for the electrochemical investigations were prepared by mixing a slurry of 80% (w/w) of active material, 10% (w/w) of Super C65 carbon black (TIMCAL) as conductive additive, and 10% (w/w) of poly(vinylidene difluoride) (Sigma-Aldrich) as binder in an adequate amount of *N*-Methyl-2-pyrrolidone (NMP) as a solvent for the slurry. The prepared slurry was coated on aluminum foil with a wet thickness of 150 μm using a doctor blade coater. The coated foil was then dried at 80 °C overnight. The dried foil was then punched into discs of 13 mm diameter and pressed with a pressure of 5 tons by using a hydraulic press. Finally, the electrodes were dried in a glass oven (Buchi) at 110 °C for 12 h and transferred to an Ar-filled glove box (MBRAUN).

The electrochemical investigations of prepared electrodes were carried out in sodium-half cells. Coin cells (CR2032) were assembled by using sodium metal (Alfa Aesar) as the reference and counter electrodes, a solution of 1 M $NaClO_4$ (Sigma-Aldrich) in EC/PC (1:1) (Sigma-Aldrich) with 2% FEC (Sigma-Aldrich) as the electrolyte, and a Whatman glass microfiber filter paper with a diameter of 18 mm as separator.

A BCS-805 multichannel battery cycler (Biologic) with a computer-controlled BT-Lab program was used for all the electrochemical investigations. All the potentials reported in this work are given vs Na^+/Na couple. The cyclic voltammetry (CV) measurements were performed in voltage ranges, 1.5−4.0 and 1.5−4.5 V at a scan rate of 0.1 mV s^{-1}, and all the galvanostatic experiments were conducted in voltage ranges of 1.5−4.0 and 1.5−4.5 V with selected C-rates. The C-rate calculation was done considering 1C as 135 mA g^{-1}. CV studies, at different scan rates from 0.1 to 1.0 mV s^{-1}, were carried out in a voltage range of 1.5−4.0 V vs Na^+/Na to determine the diffusion coefficient.

The *in operando* electrochemical investigations were performed in dedicated coin cells with Kapton windows, assembled using the LS-NMNF electrodes 1 M $NaClO_4$ in EC/PC (1:1) with 5% FEC electrolyte.[38,39]

Elucidation of Electrochemical Mechanism: *In Operando* XAS Investigations. Both *ex situ* and *in operando* X-ray absorption spectroscopic investigations were completed at beamline P65, PETRA III, DESY (Germany). *Ex situ* XAS investigations were carried out in pristine LS-NMNF material for the elucidation of the bulk oxidation state of the transition metal ions in the material. For the *ex situ* measurement, the sample was mixed with cellulose and then pressed into a pellet. XAS spectra of pressed pellet were recorded at the Mn K edge, Ni K edge, and Fe K edge in fluorescence geometry.

Further, *in operando* XAS investigations of LS-NMNF in sodium half-cells were conducted to elucidate the charge compensation mechanism of layered-spinel material during electrochemical cycling using dedicated coin cells, as described in the previous section. The *in operando* XAS spectra were recorded in fluorescence geometry at the Mn K edge, Ni K edge, and Fe K edge, and time to record each spectrum was 4 min, 3 min 50 s, and 3 min 20 s, respectively, for Mn, Ni, and Fe K edge spectra. The corresponding electrochemical experiments were conducted in the voltage range 1.5−4.5 V vs Na^+/Na at C-rates: C/10 in first charge, C/7 in first discharge, and C/5 in second charge. The obtained data were further analyzed and processed by using Demeter software package based on IFEFFIT and FEFF.[40]

Elucidation of Structural Evolution: *In Operando* X-ray Diffraction (XRD) Investigations. *In operando* XRD investigations were carried out to understand the structural evolution during the sodiation and desodiation processes. The measurements were carried out using a diffractometer with an Ag X-ray source of wavelength 0.55942 Å with a Ge 111 monochromator and a Dectris MYTHEN 2 2K double detector. The acquisition time for each pattern was 20 min.[41] For this measurement, the LS-NMNF material was coated with thin carbon paper. The *in operando* electrochemical measurements were performed in the voltage range of 1.5−4.5 V at C-rates; C/15 for first charge; and C/10 for first discharge.

RESULTS AND DISCUSSION

Thermogravimetric Analysis. Figure 1 shows the thermogravimetric studies of the 350 °C preannealed LS-NMNF sample under air, from room temperature to 1000 °C at a heating rate of 10 °C per minute. An initial weight loss observed up to 115 °C could be due to the removal of adsorbed water molecules from the surface of the sample. The weight loss observed after the removal of water and up to 450 °C could be due to the decomposition of organic molecules and acetates. A small peak around 440 °C in the DTA curve and a broad hump observed at 760 °C in the TGA curve could

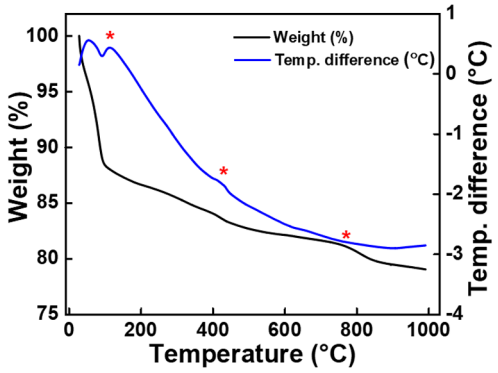

Figure 1. Thermal analysis result of the as-synthesized LS-NMNF sample, preannealed at 350 °C for 5 h.

be attributed to phase transformations at the corresponding temperatures.

Chemical Composition Analysis. The composition of the as-synthesized LS-NMNF sample was analyzed by using an optical emission spectrometer with ICP-OES, and the results are summarized in Table S1 (Supporting Information). The composition ratios obtained from the ICP-OES analysis are 0.493:0.705:0.174:0.167 (Na/Mn/Fe/Ni), which is in good agreement with the expected ratios 0.50:0.667:0.167:0.167. Note that the ratios represented here are calculated by normalizing the obtained values considering a stoichiometric Ni content.

Structural and Morphological Characterization. The XRD pattern obtained for the as-synthesized LS-NMNF at room temperature is shown in Figure 2a. The first set of

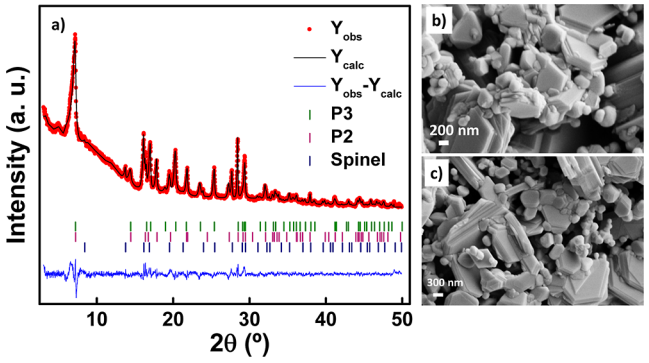

Figure 2. (a) Rietveld refinement results based on the obtained XRD pattern of the as-synthesized LS-NMNF sample and (b,c) FESEM images of the as-synthesized LS-NMNF sample.

reflections in the XRD pattern could be attributed to the P3-type crystal structure with a hexagonal lattice (space group $R\bar{3}m$; ICSD no: 261555). The next set of reflections belongs to the P2-type crystal structure having a hexagonal lattice with space group $P6_3/mmc$ (ICSD no: 231006), and the final set of reflections corresponds to the cubic spinel structure with space group $Fd\bar{3}m$ (ICSD no: 771490), which confirms the presence of the spinel phase. Hence, the coexistence of layered and spinel phases could be confirmed from the XRD result.[32,33] Manthiram et al. reported a layered-spinel cobalt-containing composite, wherein they propose that spinel phase formation could be due to the limited sodium source.[31] The layered phase could be formed from the available sodium content, and the rest of the transition metals together with oxygen may form spinel $Ni_{0.5}Co_{0.5}Mn_2O_4$. Similarly, a Fe analogue of the spinel, $Ni_{0.5}Fe_{0.5}Mn_2O_4$, is expected herein. The structural parameters obtained from the Rietveld refinement analysis, based on the obtained XRD patterns of the layered and spinel phases in the composite material, are summarized in Tables 1 and 2. The χ^2 value obtained for the Rietveld refinement results based on the powder XRD pattern of LS-NMNF is 2.23. The phase fractions of layered P3-type, P2-type, and spinel phases in the composite material are 51(3), 30(2), and 18(1)%, respectively.

FESEM images of the LS-NNMF composite cathode material are displayed in Figure 2b,c. Particles with well-defined edges along with intergrown particles were observed in the FESEM images. A broad distribution of particle size from 100 to 900 nm was detected. The increased particle size could be due to the higher annealing temperature. The larger particle size imparts higher tapped density and reduces surface parasitic reactions compared to nanosized particles. Several particles with a smooth surface were observed, and their edges looked like stacked layers. The coexistence of P2, P3, and spinel phases was further confirmed from the HRTEM images shown in Figure S1a–d. The images show three sets of lattice fringes with different values of d-spacing corresponding to (100) planes of the P2 phase (d_{100} = 0.25 nm), (003) planes of the P3 phase (d_{003} = 0.55 nm), and (111) planes of spinel (d_{111} = 0.48 nm).

X-ray Photoelectron Spectroscopy Analysis. The investigation of surface oxidation states of the transition metals present in the material was done by using X-ray photoelectron spectroscopic analysis. The Mn 2p spectrum shown in Figure S1e–g contains two sets of peaks corresponding to Mn $2p_{3/2}$ and Mn $2p_{1/2}$, separated by a spin–orbit splitting energy of ~11.72 eV. The peaks at 642.20, 653.48, 643.13, and 654.50 eV indicate the presence of Mn in a mixed oxidation state of +3 and +4.[42] The peaks at 711.7 and 724.72 eV in the Fe 2p spectrum observed in Figure S1f along with their satellite peaks at 718.52 and 733.63 eV confirm the trivalent surface oxidation state of iron.[43−45] The +2 oxidation state of nickel was also confirmed from the XPS analysis by fitting the spectrum with peaks at 854.84 and 872.59 eV along with the satellite peaks at 860.66 and 879.04 eV.[43,45,46]

Electrochemical Studies. The electrochemical activity of transition metals in LS-NMNF was analyzed by CV studies at a scan rate of 0.1 mV s^{-1}. The results obtained for CV, conducted in the voltage range 1.5–4.0 V, are shown in Figure 3a. In the first cycle, an oxidation peak appears at 3.79 V and the corresponding reduction peak is observed at 3.48 V. These peaks appearing in the voltage range 3.0–4.0 V could be due to the redox reaction; $Ni^{2+} \rightleftharpoons Ni^{3+} \rightleftharpoons Ni^{4+}$[31−33] (denoted by 2 and 2* in the charge and discharge processes, respectively). From the second cycle onward, the oxidation peak shifted to a lower value of 3.70 V and the reduction peak shifted to a higher value of 3.59 V. The shift of the anodic peak to a lower voltage and cathodic peak to a higher voltage is attributed to decreased polarization due to better kinetics.[47] The peak current corresponding to the redox reaction of Ni after the first cycle appeared to be constant, indicating its higher reversibility. From the CV curves obtained in the voltage range 1.5–4.0 V, the redox activity corresponding to Mn^{4+}/Mn^{3+} reaction was observed below 3.0 V[32,33] (denoted by 1 and 1* for the charge and discharge processes, respectively). The higher peak current observed in the Mn^{4+}/Mn^{3+} redox activity region in comparison with that obtained in the Ni^{4+}/Ni^{2+} redox activity region implies that the redox activity of Mn

Table 1. Rietveld Refinement Results based on Obtained XRD Data of LS-NMNF Material; Structural Parameters of Layered (P2 and P3) and Spinel Phases are Summarized

phase	Wyckoff site	X	Y	Z	unit cell parameters (Å)			unit cell volume (Å^3)
					a	b	c	
P3	$[Mn]_{3a}$	0	0	0	2.8794(4)	2.8794(4)	16.932(6)	121.58(5)
	$[Fe]_{3a}$	0	0	0				
	$[Ni]_{3a}$	0	0	0				
	$[Na]_{6c}$	0	0	0.154(5)				
	$[O]_{6c}$	0	0	0.394(1)				
P2	$[Mn]_{2a}$	0	0	0	2.8798(4)	2.8798(4)	11.273(3)	80.97(3)
	$[Fe]_{2a}$	0	0	0				
	$[Ni]_{2a}$	0	0	0				
	$[Na]_{2b}$	0	0	1/4				
	$[Na]_{2d}$	1/3	2/3	3/4				
	$[O]_{4f}$	1/3	2/3	0.079(4)				
spinel	$[Mn]_{16d}$	1/2	1/2	1/2	8.364(1)	8.364(1)	8.364(1)	585.2(1)
	$[Fe]_{8a}$	1/8	1/8	1/8				
	$[Ni]_{16d}$	1/2	1/2	1/2				
	$[O]_{32e}$	0.252(7)	0.252(7)	0.252(7)				

Table 2. Rietveld Refinement Results based on Obtained XRD Data of LS-NMNF Material; Phase Fractions of Various Phases in the As-synthesized LS-NMNF Material

phase	space group	phase fraction (%)
P3	$R\bar{3}m$	51(3)
P2	$P6_3/mmc$	30(2)
spinel	$Fd\bar{3}m$	18(1)

species predominates in the system. As the cycle number increases, the redox peaks of Mn move to higher voltages, and this could be due to structural rearrangements of layers occurring during cycling.

The results obtained for CV investigations carried out in the voltage range of 1.5−4.5 V are displayed in Figure 3b. In addition to the peak corresponding to $Ni^{2+} \rightarrow Ni^{4+}$ reaction (denoted by 2), observed for the CV studies carried out in voltage range 1.5−4.0 V, the CV curves obtained in the voltage range 1.5−4.5 V displayed the appearance of a peak around 4.2 V (denoted by 3), the intensity of which continuously decreased in the subsequent cycles. A corresponding reduction peak "3*" was observed in the following discharge around 3.66 V, which continuously shifted to lower voltages in the following cycles, seen as shoulders of peak "2*". The origin of this set of peaks could be the Fe^{4+}/Fe^{3+} electrochemical activity of Fe in the sample. Similar to the CV conducted with the upper cut-off voltage of 4.0 V, the CV carried out with the upper cut-off voltage of 4.5 V displayed the redox peaks 1 and 1*, corresponding to the Mn^{4+}/Mn^{3+} electrochemical reaction. Hence, to understand the electrochemical reactions in detail, a wider voltage window of 1.5−4.5 V was chosen for the *in operando* investigations.

To investigate the sodium storage performance of LS-NMNF, galvanostatic charge−discharge studies were conducted at C/10 (1C = 135 mA g^{-1}, calculated taking the initial amount of Na in the nominal composition into account). The results obtained from the studies conducted in the voltage range 1.5−4.0 and 1.5−4.5 V are given in Figure 4a, and the corresponding voltage profiles are shown in Figure 4b,c. The initial charge capacity and discharge capacity of LS-NMNF are observed to be 48 and 143 mAh g^{-1}, respectively, in the voltage range of 1.5−4.0 V. Note that the charge capacity is very low in the first cycle due to the absence of redox activity of Mn in the first charge since the majority of manganese ions exist in the +4 oxidation state. From the second cycle onward, the Coulombic efficiency was stabilized to ∼100%, which indicates greater reversibility of the system. At the 50th cycle, the LS-NMNF material showed a discharge capacity of 105 mAh g^{-1} with a capacity retention of 73.4%.

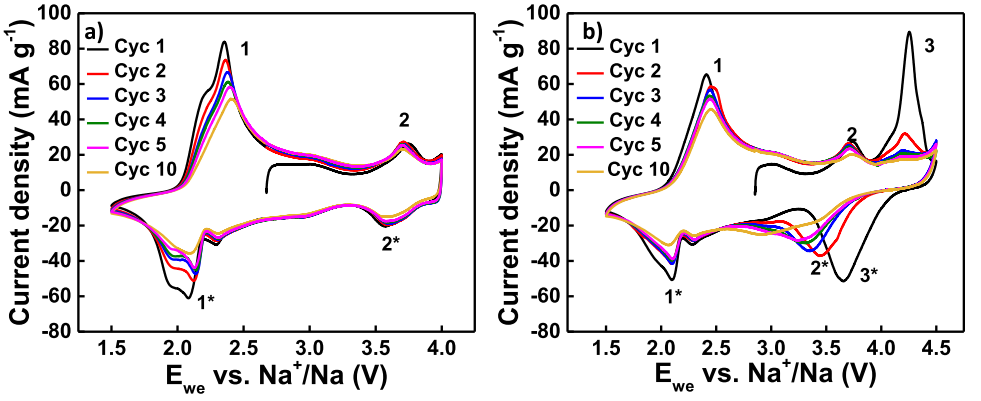

Figure 3. Cyclic voltammogram of LS-NMNF, carried out at a scan rate of 0.1 mV s^{-1} in the voltage range (a) 1.5−4.0 and (b) 1.5−4.5 V.

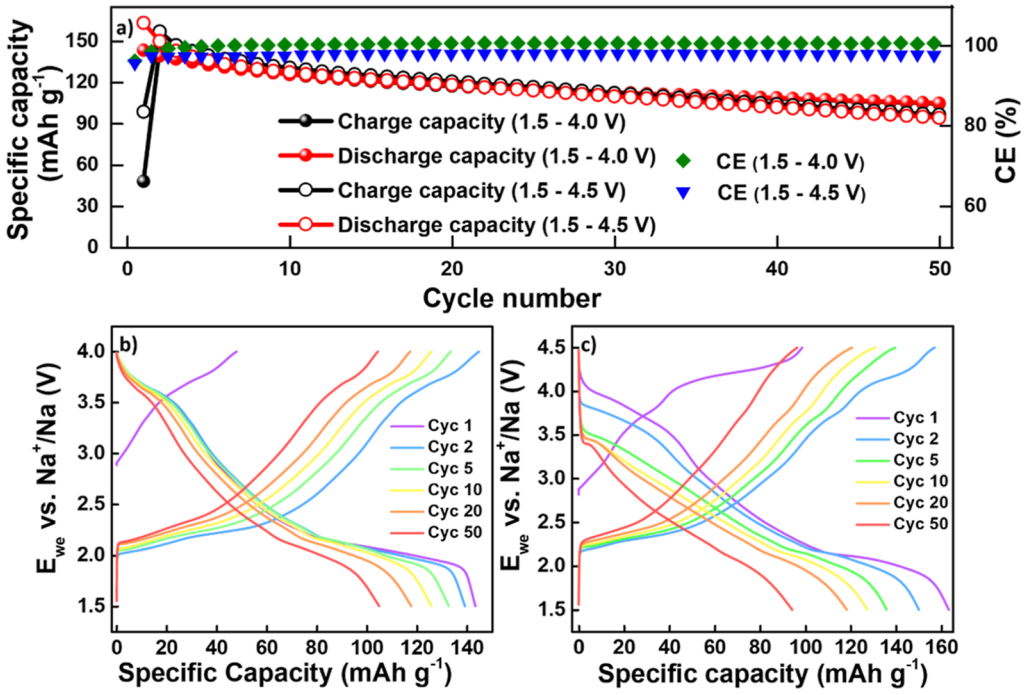

Figure 4. Charge−discharge behavior of LS-NMNF in a sodium half-cell at C/10 with 1 M $NaClO_4$ in EC/PC (1:1 v/v) electrolyte with an FEC electrolyte additive (2% v/v). (a) Cycling performance for 50 cycles in the voltage range 1.5−4.0 and 1.5−4.5 V. Voltage profiles correspond to the cycling stability studies, conducted in the voltage window (b) 1.5−4.0 and (c) 1.5−4.5 V.

The voltage profiles of LS-NMNF are shown in Figure 4b. In the first charging, a plateau is observed around 3.70 V, which corresponds to the oxidation of Ni^{2+}. The voltage profile of first charging does not show the electrochemical activity of Mn because most of the Mn in the material is in +4 oxidation state. On first discharging, the plateau near 2.0 V indicates the reduction of Mn^{4+} to Mn^{3+}. From the second cycle onward, two plateaus appear around 2.10 and 1.95 V in the charge and discharge, respectively, corresponding to the redox activities of Mn^{4+}/Mn^{3+}. Further, two plateaus observed around 3.70 V on charging and discharging correspond to the electrochemical activity of Ni^{4+}/Ni^{2+}, which is in good accordance with the CV results. From the voltage profile, the voltage corresponding to manganese oxidation increases with the increasing cycle number, which is in agreement with the CV results. The smooth curves at higher voltages suggest that the presence of Fe in LS-NMNF minimizes the Na/vacancy ordering and thereby imparts facile phase transformation.[48] The material delivered an initial charge capacity of 98.6 mAh g^{-1} in the potential window of 1.5−4.5 V and a corresponding discharge capacity of 163.4 mAh g^{-1}. The majority of the manganese ions in the material are in the +4 oxidation state, which imparts the lower initial charge capacity. The maximum Coulombic efficiency (after first cycle) of the material was limited to 97.8% in the voltage range of 1.5−4.5 V, and the capacity retained by the material after 50 cycles was 57.6% of the initial discharge capacity, which is lower in comparison with the galvanostatic cycling results obtained in the potential window 1.5 to 4.0 V. The charge−discharge curves for the galvanostatic measurements with higher upper cutoff voltage of 4.5 V show multiple plateaus, which is in concurrence with the peaks observed in the CV curves. This could be attributed to the Fe^{4+}/Fe^{3+} electrochemical reaction and associated phase transformations. A severe voltage fade is observed when going to 50 cycles, as revealed from the voltage profile shown in Figure 4c, which could be due to irreversible parasitic reactions occurring at higher voltages such as electrolyte decomposition, structural transformation, and so forth, leading to Na loss.

Due to the better electrochemical behavior observed in the voltage range of 1.5−4.0 V, the rate capability studies of this material were carried out in this range, by increasing the discharge rates from C/10 to 5C. The obtained results are displayed in Figure 5a,b. Note that for the rate capability investigation, the charge rate was kept constant at C/10. The material exhibits reversible capacities of 126, 110, 99, 89, and 73.8 mAh g^{-1} at C-rates of C/5, C/2, 1C, 2C, and 5C, respectively. Note that the capacity obtained at a 5C discharge rate is 50.6% of the capacity obtained at C/10, which is a promising value compared to the results of Co-free materials reported in literature.[49] This superior rate performance of LS-NMNF could be contributed by the spinel component due to its high electronic conductivity (in the order of 10^{-3}−10^{-4} S cm^{-1} at room temperature) than the LTMOs.[50,51] Hence, this incorporated spinel phase would grease the wheels for timely electron transfer, which translates to a faster Na^+ diffusion in the composite material.[31−33] The 2 V plateau is found to disappear at high C-rates in the voltage profiles corresponding to the rate capability studies due to increased polarization, probably originating from a kinetically limited reaction mechanism involving multiple phase transformations.[52]

The LS-NMNF sample was subjected to a high-rate cycling study, and the results are displayed in Figure 5c. In this study, the charge and discharge rates were fixed as C/10 and 1C, respectively. The material delivered a discharge capacity of ~120 mAh g^{-1} in the initial cycle. At the 100th cycle, the material shows a discharge capacity of 83 mAh g^{-1} with a capacity retention of 69%. Moreover, after the second cycle, the Coulombic efficiency remains >99% throughout the cycling. A close look at the voltage profile (Figure 5d) reveals a voltage decay around 2.0 V, which could further point out

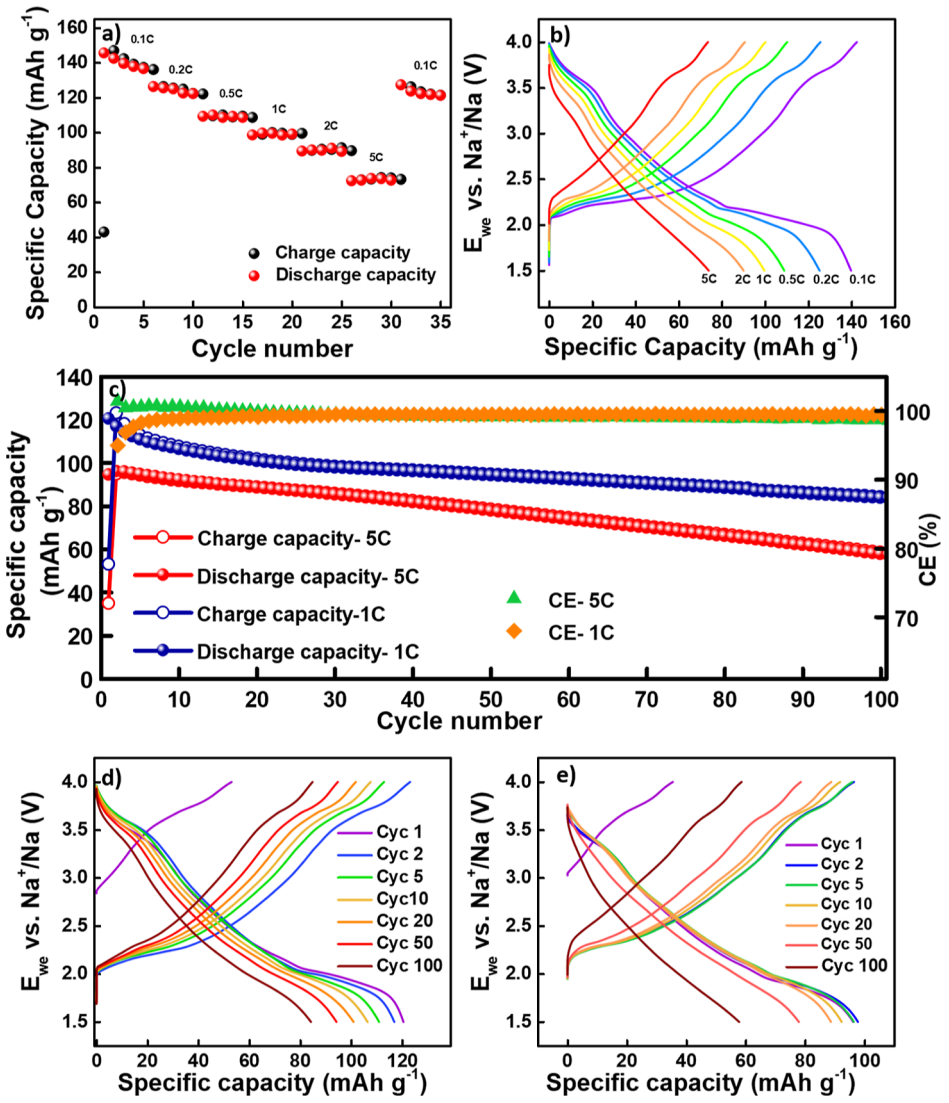

Figure 5. (a) Specific capacity vs cycle number plots of LS-NMNF in a sodium half-cell (voltage range 1.5−4.0 V at RT) at C/10 charge rate and varied discharge rates. (b) Corresponding charge−discharge curves. (c) Specific capacity vs cycle number plots obtained from the high-rate cycling stability studies of the LS-NMNF sample at 1C and 5C (1.5−4.0 V vs Na^+/Na). (d) Charge−discharge curves of LS-NMNF in a sodium half-cell at 1C. (e) At 5C.

the kinetic limitation of the Mn^{4+}/Mn^{3+} electrochemical reaction. This could also indicate a possibility of the Mn^{3+} disproportionation reaction (to Mn^{4+} and Mn^{2+}), which would eventually lead to Mn dissolution in the electrolyte. Nevertheless, the better high-rate performance, which is observed in this layered-spinel composite could be assigned to the incorporated spinel component, which improves the overall reaction kinetics by increasing the electronic conductivity and the enhanced structural stability due to the merging of P3 and P2 components. Further, the high-rate cycling studies at a discharge rate of 5C are displayed in Figure 5c,e. The material exhibits an initial discharge capacity of 94 mAh g^{-1} and a capacity retention of 61% at the 100^{th} cycle. These results again confirm the enhancement of electrochemical performance via the triphasic strategy. The superior electrochemical performance exhibited by the material could be attributed to the approach of compositing three phases P2, P3, and spinel. While the P3 phase contributes to the higher reversible capacity, the open diffusion channels present in the P2 phase provide faster diffusion of Na^+ ions. Further, the intrinsically high electronic conductivity of the spinel phase improves the overall Na-ion diffusion kinetics. The diffusion coefficient D_{Na^+} is calculated by conducting CV at different scan rates in a voltage window of 1.5−4.0 V vs Na^+/Na (Figure S2). The peak current of the redox peaks was found to increase with the increase in the scan rate, and the linear relationship between the peak current and square root of scan rate implies a diffusion-controlled behavior during sodium extraction and intercalation. From the CV experiment, the diffusion coefficient value is obtained as 1.48×10^{-10} cm s^{-1}, which is similar to that reported for cobalt-based layered-spinel composite cathode materials.[26,29,31]

***In Operando* X-ray Absorption Studies.** To get the information regarding bulk oxidation states of transition metals in the pristine LS-NMNF sample, X-ray absorption near edge structure (XANES) measured at K edges of Mn, Fe, and Ni and those of different reference materials were compared (Figure S3). The XANES Mn K edge spectrum of the pristine sample is compared with those of references Mn_2O_3 and MnO_2. The position of the Mn K edge spectrum of the pristine

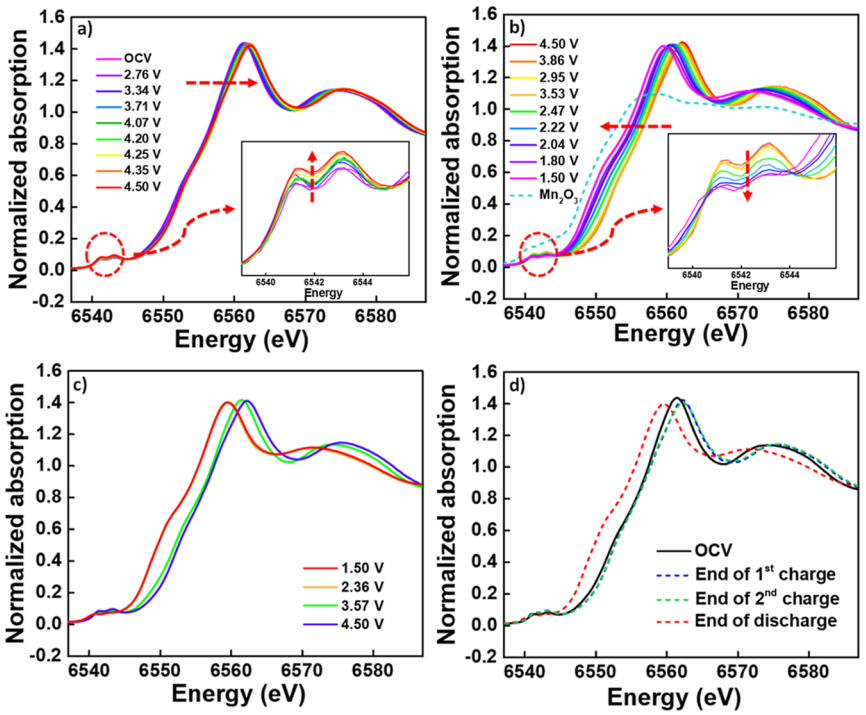

Figure 6. Na/LS-NMNF cell; XANES Mn K edge spectra (a) during the first charging. (b) During first discharging. (c) Na/LS-NMNF cell; XANES Mn K edge spectra during second charging. (d) Comparison of the XANES Mn K edge spectrum at the OCV, end of first charge, and end of second charge.

sample lies at higher energies than that of Mn_2O_3 and slightly less than that of MnO_2, indicating that the major bulk oxidation state of Mn is +4 in the sample, with slight contribution from Mn^{3+}. A minor amount of Mn^{3+} is usually present in LTMOs due to the oxygen loss during the high temperature synthesis process.[53,54] This result agrees with the XPS fitting results, as it indicates the presence of a minor amount of Mn^{3+} in the material, even though XPS gives information on the surface oxidation states and not bulk. The position of the Fe K edge in the XANES region overlaps with that of the reference sample Fe_2O_3, indicating a bulk oxidation state of +3 for Fe in the LS-NMNF pristine sample. The position of Ni K edge in the XANES of LS-NMNF material overlaps with that of the NiO reference sample, implying a bulk oxidation state of +2 for Ni in the material.

In order to study the charge compensation mechanism and to elucidate the electrochemical mechanism of the LS-NMNF material, *in operando* X-ray absorption spectroscopic studies were carried out. Mn, Fe, and Ni K edge spectra were recorded on a Na/LS-NMNF half-cell during the first cycle and second charge in the voltage range of 1.5−4.5 V. The voltage profiles of the electrochemical cycling during the *in operando* measurement are displayed in Figure S4, and the corresponding differential capacity versus voltage curve is shown in Figure S5. The dQ/dV plots in the voltage range of 1.5−4.5 V show a similar behavior to CV in the voltage range of 1.5−4.5 V and the obtained specific capacity values for the first cycle and subsequent discharge are comparable with that of the galvanostatic experiments conducted at the voltage range 1.5−4.5 V. The XANES corresponding to the Mn K edge of LS-NMNF material during first charging is shown in Figure 6a. A minor shift in the edge position is observed during the charging process, which could be due to the oxidation of residual Mn^{3+} present in the material. The intensity of the XANES pre-edge feature of Mn K edge was also found to increase with increase in charging potential. However, the white line intensity remains the same. Therefore, the increase in pre-edge intensity on charging could be due to the oxidation of minute amount of Mn^{3+} to Mn^{4+}.[52] In contrast, the edge position corresponding to Mn K edge XANES shifted continuously toward the lower energy during discharging. Concurrently, the pre-edge intensity was also found to decrease, with no significant changes in the white line intensity. This reveals the intercalation of an additional number of moles of Na^+ ions than initial stoichiometry, accompanied by reduction of Mn^{4+} to Mn^{3+}. Nevertheless, the position of Mn K edge XANES corresponding to the fully discharged state (1.50 V vs Na^+/Na) did not overlap with that of the Mn K edge position corresponding to reference material Mn_2O_3. This indicates an incomplete reduction of Mn^{4+} to Mn^{3+} with the insertion of Na^+.[55−57]

In the extended X-ray absorption fine structure (EXAFS) Fourier transform (FT), displayed in Figure S6, peaks around 1.5 Å correspond to the first scattering shell of the transition metal−oxygen (TM−O) bond, and peaks around 2.5 Å correspond to the transition metal−metal (TM−M; M can be TM and Na) bond within the layer. The EXAFS-FT of Mn K edge on charging shows a decrease in the intensity of the peak corresponding to the Mn−M coordination shell (Figure S6a), and this could be due to the decrease in the sodium content in the alkali metal layer during sodium extraction; another reason could be the formation of vacancies in the transition metal layer. On discharging, the intensities of both peaks, Mn−O and Mn−M decrease, and this could be due to the Jahn−Teller distortion arising from Mn^{3+} species formed on discharging.

During the second charging, the Mn K edge position shifts toward higher energy, indicating the oxidation of Mn^{3+} to Mn^{4+} (Figure 6c). The XANES spectrum of Mn K edge of LS-

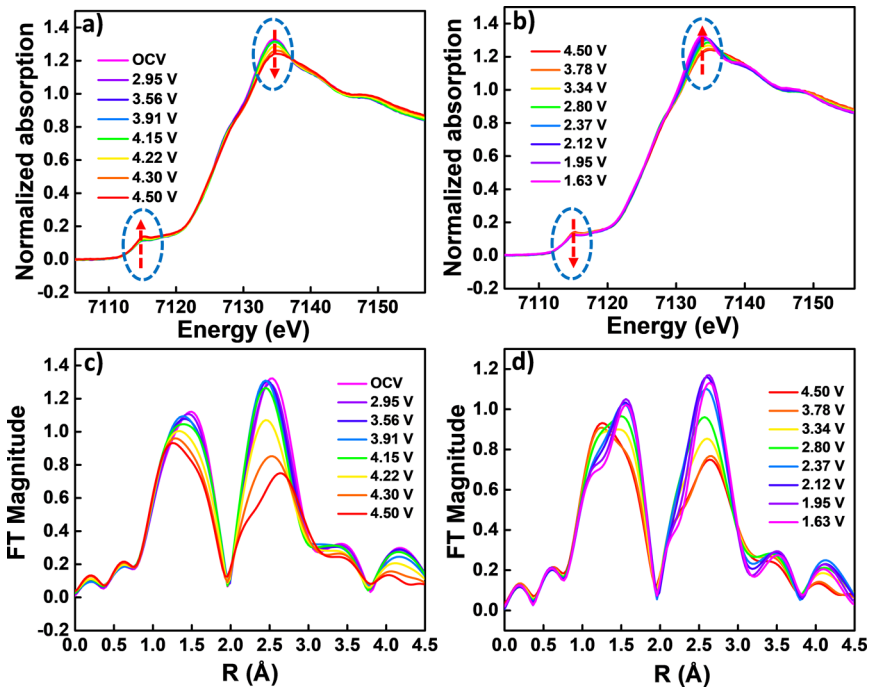

Figure 7. Na/LS-NMNF cell; XANES Fe K edge spectra (a) during the first charging. (b) During first discharging. (c) EXAFS FT during charging. (d) EXAFS FT during discharging.

NMNF at the end of the first charge and the second charge shows similar features, which indicates the reversibility of the system during electrochemical cycling (Figure 6d). The difference in the edge position of the Mn K edge at the end of discharge (EOD) and the OCV shows that the initial bulk oxidation was close to Mn^{4+}, whereas at the EOD, the bulk oxidation state was reduced and shifted close to Mn^{3+}.

The XANES Fe K edge spectra of LS-NMNF during initial charging and discharging are shown in Figure 7a,b. No major shift is observed in the position of the Fe K edge XANES during the entire cycle. However, a shift to higher energy was observed for the edge near the white line region of XANES on charging and the intensity of the pre-edge feature corresponding to Fe K edge XANES was found to increase with a decrease in white line intensity. The increase in pre-edge intensity and the decrease in white line intensity point to a structural distortion, which could be attributed to the Jahn−Teller distortion arising from the presence of Fe^{4+}, resulting from the oxidation of Fe^{3+}, further confirming the Fe^{4+}/Fe^{3+} redox activity around 4.22 V.[58−60] Another reason could be the migration of Fe from the octahedral site of the transition metal layer to the tetrahedral site of the alkali metal layer.[61] To obtain more details about the local coordination changes, the EXAFS region of the LS-NMNF material during electrochemical cycling is further analyzed. The changes in the average radial distribution around Fe are shown in Figure 7c,d. Considering that the spectra are not phase-corrected, the *R* values in the EXAFS region shown here will be slightly shorter than the original bond length. Figure 7c shows that the FT amplitude corresponding to Fe−O and Fe−M around 1.5 and 2.5 Å, respectively, in the EXAFS FT of Fe K edge is decreasing on charging, and this could be due to distortion around iron on Na^+ extraction and/or Jahn−Teller distortion of Fe^{4+}. The decrease in the FT amplitude of the peak of the Fe−TM coordination shell indicates the formation of vacancies in the transition metal layer. These changes start to appear from the spectra recorded from 4.22 V, indicating that the electrochemical activity of Fe takes place above 4.00 V. This is in concurrence with the peak observed in the CV (carried out in the voltage range 1.5−4.5 V), around 4.20 V. In addition to that, the peak corresponding to Fe−M coordination shell at the end of charge (EOC) shifts to a radial distribution value higher than that of OCV, which further indicates a change in the local structure around iron metal. The increase in Fe−M average radial distance could be attributed to the transformation of a part of Fe−Fe edge sharing octahedral environment to corner sharing due to the migration of iron from transition metal layer to alkali metal layer.[62,63]

Further, the EXAFS FT spectra at OCV, EOC, and EOD were compared, as shown in Figure S7. The peak corresponding to the Fe−O coordination shell was observed at 1.50 Å, when the cell was at the OCV, and at the EOC, it was shifted to a lower *R* value, indicating the oxidation of Fe^{3+} to Fe^{4+}.[58,59] At the EOD, the peak corresponding to the Fe−O coordination shell was again shifted to a higher *R* value, which implies the reduction of Fe^{4+} to Fe^{3+}. The difference in the *R*-value corresponds to the Fe−O coordination shell at OCV, EOC, and EOD, which further confirms the oxidation of Fe^{3+} to Fe^{4+} during charging and reduction of Fe^{4+} to Fe^{3+} during discharge.

On discharging, the changes happening at the XANES Fe K edge revert with an increase in the white line intensity and decrease in pre-edge intensity (Figure 7b). In EXAFS FT, the intensities of the Fe−O peak and Fe−TM peak were increased until 2.12 V, denoting the reduction of Fe^{4+}. Further, the shifted peaks corresponding to the Fe−M coordination shell revert to a lower radial distribution value when the discharging voltage decreases (Figure 7d). This indicates a reversible change in the local coordination of Fe back to edge sharing octahedra. However, a decrease in the FT amplitude of the Fe−M peak is observed below 2.0 V and that could be due to any phase changes occurred during intercalation of sodium

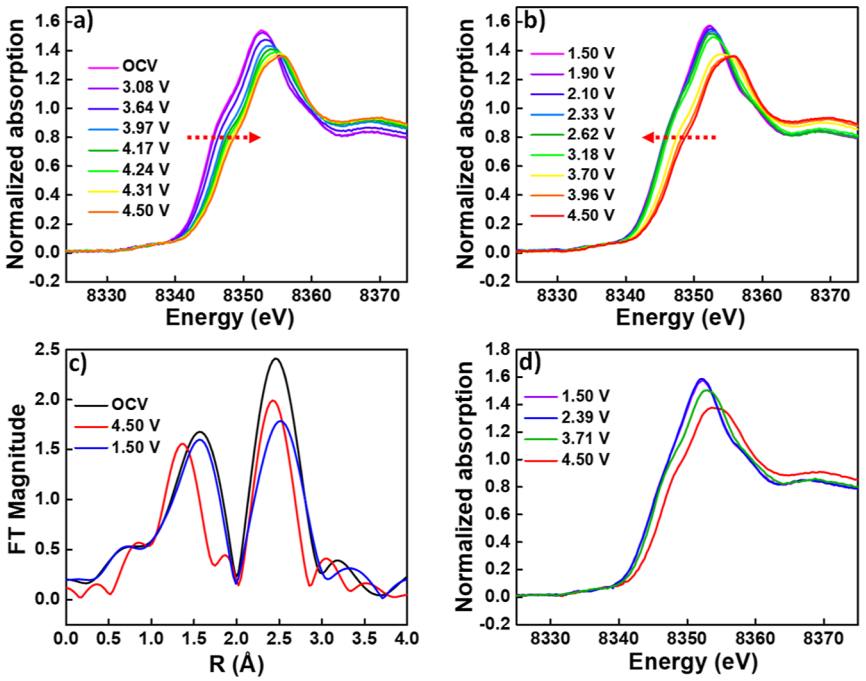

Figure 8. Na/LS-NMNF cell; XANES Ni K edge spectra (a) during the first charging. (b) During first discharging. (c) EXAFS FT at OCV, EOC, and EOD. (d) XANES Ni K edge spectra during the second charging.

ions below 2.0 V. In addition to that, the FT amplitude of the peak obtained at the EOD is less than that of OCV, indicating an incomplete electrochemical reaction at the EOD (Figure S7).[61]

The normalized pre-edge intensities of the XANES Fe K edge of LS-NMNF at the open circuit voltage (OCV), EOC, and EOD are displayed in Figure S8. On carefully analyzing the Fe K edge spectra, it is observed that on charging, the pre-edge intensity increases, and on discharging, the pre-edge intensity decreases. Interestingly, the pre-edge intensity at the EOD is higher than the pre-edge intensity at OCV, which further implies the incompletion of the electrochemical reactions. The reason behind this could be irreversible Fe^{4+} migration from the octahedral site to the vacant sodium site with increased state of charge at higher upper cutoff voltages. Such Fe migration is already reported in the literature for layered Na-ion cathodes.[58,61,62] Note that these changes in pre-edge intensity start at a voltage of around 4.20 V, and hence, limiting the upper cutoff voltage to 4.00 V will relatively reduce the irreversible reactions. In a voltage window of 1.50 to 4.00 V, Fe can act as a pillar ion, contributing only to the structural stability during cycling.[64,65] The Fe K edge spectra of LS-NMNF on second charging and the corresponding EXAFS FT spectra are shown in Figure S9. The spectra show behavior similar to that of the first charging, which suggests a similar electrochemical charge compensation mechanism for the Fe^{4+}/Fe^{3+} reaction.

The Ni K edge XANES spectra of the first cycle, second charge, and EXAFS spectra of the first cycle are displayed in Figure 8a–c. The change in the position of the Ni K edge to higher energies indicates the change in the oxidation state of Ni from +2 to +4 on charging. During the discharge process, the edge position is returned to lower energies, implying the reduction of Ni^{4+} to Ni^{2+}. It is to be noted that the white line intensity decreases when the charge voltage increases, and the white line intensity increases on discharging. These changes in the white line intensity could be due to the reversible distortions around the NiO_6 octahedra during the charging process. The peak corresponding to the Ni–O bond in EXAFS FT also confirms the redox reaction $Ni^{2+} \rightleftharpoons Ni^{4+}$ on electrochemical cycling. At the EOC, the *R* value for Ni–O bond reduces, indicating the oxidation of Ni^{2+}, and at the EOD the peak shifts back to the initial value indicating the reduction of Ni^{4+}. On analyzing the Ni K edge XANES spectra of the second charge process (Figure 8d), the oxidation of Ni from Ni^{2+} to Ni^{4+} is again observed. The comparison of Ni K edge XANES at the end of the first charge and second charge is shown in Figure S10. Note that the position of Ni K edge XANES at the end of second charge is at lower energies than that of first charge. This indicates that the extent of Ni^{2+} oxidation is lower at the end of the second charge, further indicating an incomplete electrochemical reaction.

***In Operando* XRD Studies.** *In operando* XRD studies were carried out to understand the structural evolution of LS-NMNF during electrochemical cycling in Na half-cells in the voltage range 1.5–4.5 V (Figure S11). The *in operando* XRD results are shown in Figure S12, and the selected 2θ ranges are given in Figure 9. The *in operando* XRD patterns show that the reflections corresponding to the spinel phase do not change during the entire cycle, confirming the electrochemical inactivity of the spinel phase during the electrochemical cycling. The role of the spinel phase could then be assigned to enhance the electronic conductivity and structural stability during cycling. In the case of P2/P3 phases, the change of reflection positions corresponding to 00*l* planes during sodiation and desodiation is attributed to variations in the interlayer spacing. On charging, the reflections corresponding to (002) planes of P2 initially move toward lower 2θ values, whereas the reflections corresponding to P2(102), P2(110), and P2(112) planes move to higher angles. This indicates the expansion of the unit cell in the "*c*" direction and contraction of the unit cell in the "*a*" direction during the initial

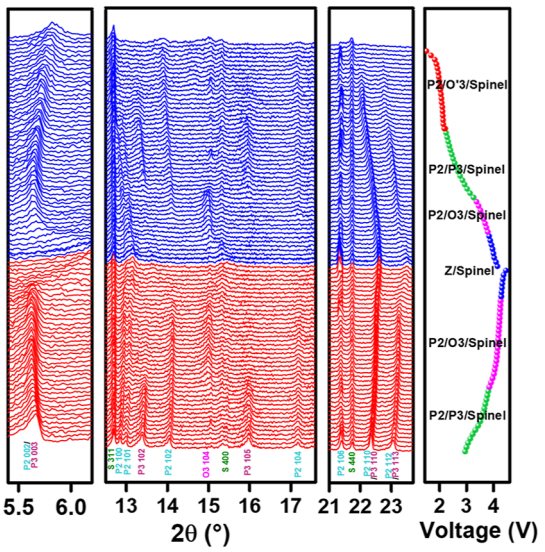

Figure 9. Selected 2θ regions of the *in operando* powder diffraction patterns of the Na/LS-NMNF cell during the first cycle in the voltage range of 1.5−4.5 V. In the XRD pattern, the red lines correspond to charge process, and the blue lines correspond to discharge processe, respectively.

desodiation. The reflections corresponding to (105) and (102) planes of the P3 phase start to disappear at 3.86 V and a new reflection related to the (104) plane of the O3 (space group $R\bar{3}m$) starts to evolve. This confirms the phase transformation of P3 to O3. Around 4.20 V, the P2 002 reflection starts to fade, and a new 003 reflection of the new phase starts to emerge, which indicates a partial P2−O2 phase transformation, where the new phase is termed "Z-phase (space group $R\bar{3}m$)". However, above 4.30 V, the reflection associated with the O3 phase transforms (together with the P2 phase) to the broad reflections of Z phase, a phase with some level of amorphization and disorder where Na^+ ions occupy both prismatic and octahedral sites, on further sodium extraction.[66] On discharging, at the initial stages of sodium intercalation, the Z phase transforms back to the O3 phase at 3.94 V and to the P2 phase at a discharging voltage of 3.85 V. Subsequently, when the discharging voltage reaches 3.03 V, the O3 phase transforms to the P3 phase and reaches the initial triphasic composition of P2/P3/Spinel. Further sodiation around 2.09 V induces the transformation from P3 to the O′3 phase (space group $R\bar{3}m$). However, transformations such as P2 to P′2, generally occurring during the electrochemical cycling of P2-type electrode materials, are not observed in the *in operando* XRD analysis during discharging, which implies that these transformations were suppressed by the intergrowth of P2, P3, and spinel. The Rietveld refinement results of Na/LS-NMNF at the OCV, 3.8 V, 4.5 V, and 1.5 V are shown in Figure S13, and the corresponding unit cell parameters are displayed in Table S2.

CONCLUSIONS

A cobalt-free spinel-integrated P2/P3 layered material is synthesized by the sol−gel method. The formation of three phases was confirmed by XRD. The material delivered a promising initial discharge capacity of 143 mAh g^{-1} and displayed capacity retention of 73% at the 50th cycle, in the voltage range of 1.5−4.0 V, when cycled at C/10. Further, the material delivered a discharge capacity of 163.4 mAh g^{-1} in a potential window of 1.5−4.50 V and exhibited a capacity retention of 57.6% of the initial discharge capacity at 50th cycle. The galvanostatic charge−discharge studies in the voltage range 1.5−4.5 V reveal that the material delivers poor electrochemical performance in sodium half-cells above 4.00 V due to the irreversible parasitic reactions and multiple phase transformations in that voltage range. Moreover, the material delivered a discharge capacity of 72 mAh g^{-1} at 5C (voltage range; 1.5−4.0 V), which is 50.6% of the capacity obtained at C/10. In the long term high-rate cycling studies at 1C, the layered spinel material showed a discharge capacity of ∼120 mAh g^{-1} in the initial cycle and 83 mAh g^{-1} in the 100th cycle with a capacity retention of 69% (voltage range; 1.5−4.0 V). This excellent behavior of the material shows that the three phases present in the material enhance the electrochemical performance synergistically. The P2/P3 layered phase imparts a smoother faster diffusion pathway for sodium ions, and the incorporated spinel phase increases the electronic conductivity of the material, thereby coordinating the sodium diffusion and electron transfer. To understand the charge compensation mechanism during electrochemical cycling, *in operando* X-ray absorption spectroscopic investigations were carried out in the voltage range 1.5−4.5 V. It was observed that on charging, Mn^{3+} oxidizes to Mn^{4+} and Ni^{2+} oxidizes to Ni^{4+} and on discharging the reverse reactions take place. Fe^{3+} remains inactive up to 4.00 V and oxidizes to Fe^{4+} at 4.22 V with simultaneous changes in the local structure. The change in the pre-edge feature and EXAFS of Fe K edge during cycling could be attributed to Fe^{4+} migration from octahedral sites to the alkali metal layer. The structural evolution during the electrochemical cycling was investigated by *in operando* XRD. It is observed that the spinel phase remains electrochemically inactive during the entire cycling process. The P3 phase

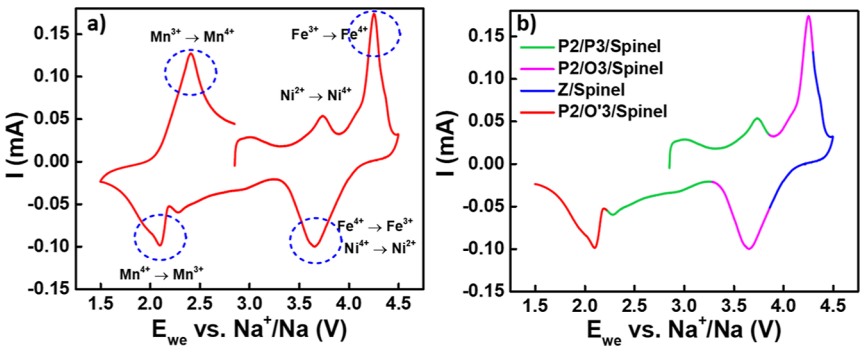

Figure 10. Summary of the electrochemical mechanism elucidated from (a) *in operando* XAS and (b) *in operando* XRD.

transforms to the O3 phase during the charging process. With the increasing potential, the P2 phase, together with the O3 phase changes to the Z phase, where Na^+ ions occupy both prismatic and octahedral sites. On discharging, the Z phase transforms back to a mixture of P2 and O3 and subsequently to P2/P3. No P2−P′2 phase transition is observed when going down to lower voltages; however, P3−O′3 phase transition takes place at potential below 2 V. At the EOD, a mixture of P2, O′3 and spinel phases was observed. The overall electrochemical mechanism can be summarized as follows and the same is displayed in Figure 10.

On Charging (up to 4.5 V). Structural evolution: spinel/P2/P3 → spinel/P2/O3 → spinel/Z

Oxidation state evolution: $Mn^{3+} \rightarrow Mn^{4+}$, $Ni^{2+} \rightarrow Ni^{4+}$, above 4.20 V: $Fe^{3+} \rightarrow Fe^{4+}$

On Discharging (up to 1.5 V). Structural evolution: spinel/Z → spinel/P2/O3 → spinel/P2/P3 → spinel/P2/O′3

Oxidation state evolution: $Mn^{4+} \rightarrow Mn^{3+}$, $Ni^{4+} \rightarrow Ni^{2+}$, $Fe^{4+} \rightarrow Fe^{3+}$

ASSOCIATED CONTENT

Supporting Information

The Supporting Information is available free of charge at https://pubs.acs.org/doi/10.1021/acsami.4c01140.

X-ray photoelectron spectra of Mn 2p, Fe 2p and Ni 2p core levels of LS-NMNF; XANES Ni, Mn and Fe K edges of LS-NMNF and corresponding reference materials; electrochemical behavior of the first cycle and second charge of Na/LS-NMNF cell during *in operando* XAS measurements; EXAFS FT of Mn K edge spectra during first cycle; comparison of the Fe K edge EXAFS spectra of LS-NMNF at OCV, EOC, and EOD; the normalized pre-edge intensities of XANES Fe K edge of LS-NMNF at different states; XANES Fe K edge spectra during second charging; comparison of XANES Ni K edge spectrum at the end of first charge and end of second charge; voltage profiles of the Na/LS-NMNF cell during *in operando* XRD measurements; the *in operando* XRD patterns of Na/LS-NMNF cell during the first cycle; Rietveld refinement results based on the obtained XRD patterns of LS-NMNF in Na half-cell, from *in operando* experiment; ICP-OES measurement results; Rietveld refinement results of LS-NMNF material, from *in operando* experiments, at various voltages (PDF)

AUTHOR INFORMATION

Corresponding Authors

Ditty Dixon − *Academy of Scientific and Innovative Research (AcSIR), Ghaziabad 201002, India; School of Chemical Sciences, Mahatma Gandhi University, Kottayam 686560 Kerala, India*; Email: dittydixon@mgu.ac.in

Aiswarya Bhaskar − *Electrochemical Power Sources Division, CSIR-CECRI, Karaikudi 630003 Tamil Nadu, India; Academy of Scientific and Innovative Research (AcSIR), Ghaziabad 201002, India*; orcid.org/0000-0003-0557-5199; Email: aiswarya@cecri.res.in

Authors

Aswathi Thottungal − *Electrochemical Power Sources Division, CSIR-CECRI, Karaikudi 630003 Tamil Nadu, India; Academy of Scientific and Innovative Research (AcSIR), Ghaziabad 201002, India*

Aswinsriram Sriramajeyam − *Electrochemical Power Sources Division, CSIR-CECRI, Karaikudi 630003 Tamil Nadu, India*

Ammu Surendran − *Electrochemical Power Sources Division, CSIR-CECRI, Karaikudi 630003 Tamil Nadu, India; Academy of Scientific and Innovative Research (AcSIR), Ghaziabad 201002, India*

Harsha Enale − *Electrochemical Power Sources Division, CSIR-CECRI, Karaikudi 630003 Tamil Nadu, India; Academy of Scientific and Innovative Research (AcSIR), Ghaziabad 201002, India*

Angelina Sarapulova − *Karlsruhe Institute of Technology (KIT), Institute for Applied Materials (IAM), Eggenstein-Leopoldshafen D-76344, Germany; Freiburg Materials Research Center (FMF), Freiburg 79104, Germany; Dep. Electrical Energy Storage, Fraunhofer Institute for Solar Energy Systems, Freiburg 79110, Germany*; orcid.org/0000-0003-4643-3912

Oleksandr Dolotko − *Karlsruhe Institute of Technology (KIT), Institute for Applied Materials (IAM), Eggenstein-Leopoldshafen D-76344, Germany*

Qiang Fu − *Karlsruhe Institute of Technology (KIT), Institute for Applied Materials (IAM), Eggenstein-Leopoldshafen D-76344, Germany*

Michael Knapp − *Karlsruhe Institute of Technology (KIT), Institute for Applied Materials (IAM), Eggenstein-Leopoldshafen D-76344, Germany*; orcid.org/0000-0003-0091-8463

Notes

The authors declare no competing financial interest.

ACKNOWLEDGMENTS

A.B. acknowledges financial support from "DST-IISc Energy Storage Platform on Supercapacitors and Power Dense Devices" through the MECSP-2K17 program under grant no. DST/TMD/MECSP/2K17/20. D.D. acknowledges the financial support from the funding agency, Science and Engineering Board (SERB), New Delhi, India through Ramanujan Fellowship, under the grant number SB/S2/RJN-162/2017. A.T. gratefully acknowledges the Council of Scientific and Industrial Research (CSIR) for a Senior Research Fellowship through National Eligibility Test. A.S. is grateful to UGC New Delhi (ref. no.:63/CSIR-UGC NET DEC. 2017) for the UGC SRF grant. DESY, Hamburg, Germany is acknowledged for the beamtime allocation at the P65 beamline at PETRA III and we acknowledge the beamline scientist Dr. Edmund Welter for the support. The Central Instrumentation Facility at CSIR-CECRI is acknowledged for technical support with material characterization. This work contributes to the research performed at CELEST (Center for Electrochemical Energy Storage Ulm-Karlsruhe) and was funded by the German Research Foundation (DFG) under Project ID 390874152 (POLiS Cluster of Excellence). Dr. Thomas Bergfeldt (IAM-AWP) is gratefully acknowledged for the ICP-OES measurement. IIUCNN, MG University, Kottayam and analytical engineer Anu A.S. is gratefully acknowledged for support with TEM characterization. The CSIR−CECRI manuscript communication number is CECRI/PESVC/Pubs/2023-174.

REFERENCES

(1) Dehghani-Sanij, A. R.; Tharumalingam, E.; Dusseault, M. B.; Fraser, R. Study of Energy Storage Systems and Environmental Challenges of Batteries. *Renew. Sustain. Energy Rev.* **2019**, *104*, 192−208.

(2) Solomon, A. A.; Kammen, D. M.; Callaway, D. The Role of Large-Scale Energy Storage Design and Dispatch in the Power Grid: A Study of Very High Grid Penetration of Variable Renewable Resources. *Appl. Energy* **2014**, *134*, 75−89.

(3) Zhang, L.; Miao, J.; Li, J.; Li, Q. Halide Perovskite Materials for Energy Storage Applications. *Adv. Funct. Mater.* **2020**, *30* (40), 2003653.

(4) Stoyanova, R.; Koleva, V.; Stoyanova, A. Lithium versus Mono/Polyvalent Ion Intercalation: Hybrid Metal Ion Systems for Energy Storage. *Chem. Rec.* **2019**, *19* (2−3), 474−501.

(5) Xiang, X.; Zhang, K.; Chen, J. Recent Advances and Prospects of Cathode Materials for Sodium-Ion Batteries. *Adv. Mater.* **2015**, *27* (36), 5343−5364.

(6) Wang, P.; You, Y.; Yin, Y.; Guo, Y. Layered Oxide Cathodes for Sodium-Ion Batteries: Phase Transition, Air Stability, and Performance. *Adv. Energy Mater.* **2018**, *8* (8), 1701912.

(7) Han, M. H.; Gonzalo, E.; Singh, G.; Rojo, T. A Comprehensive Review of Sodium Layered Oxides: Powerful Cathodes for Na-Ion Batteries. *Energy Environ. Sci.* **2015**, *8* (1), 81−102.

(8) Ortiz-Vitoriano, N.; Drewett, N. E.; Gonzalo, E.; Rojo, T. High Performance Manganese-Based Layered Oxide Cathodes: Overcoming the Challenges of Sodium Ion Batteries. *Energy Environ. Sci.* **2017**, *10* (5), 1051−1074.

(9) Delmas, C.; Fouassier, C.; Hagenmuller, P. Structural Classification and Properties of the Layered Oxides. *Physica B+C* **1980**, *99*, 81−85.

(10) Lee, E.; Lu, J.; Ren, Y.; Luo, X.; Zhang, X.; Wen, J.; Miller, D.; Dewahl, A.; Hackney, S.; Key, B.; Kim, D.; Slater, M. D.; Johnson, C. S. Layered P2/O3 Intergrowth Cathode: Toward High Power Na-Ion Batteries. *Adv. Energy Mater.* **2014**, *4* (17), 1400458.

(11) Ong, S. P.; Chevrier, V. L.; Hautier, G.; Jain, A.; Moore, C.; Kim, S.; Ma, X.; Ceder, G. Voltage, Stability and Diffusion Barrier Differences between Sodium-Ion and Lithium-Ion Intercalation Materials. *Energy Environ. Sci.* **2011**, *4* (9), 3680−3688.

(12) Wang, P. F.; You, Y.; Yin, Y. X.; Guo, Y. G. An O3-Type $NaNi_{0.5}Mn_{0.5}O_2$ Cathode for Sodium-Ion Batteries with Improved Rate Performance and Cycling Stability. *J. Mater. Chem. A* **2016**, *4* (45), 17660−17664.

(13) Zhu, Y. E.; Qi, X.; Chen, X.; Zhou, X.; Zhang, X.; Wei, J.; Hu, Y.; Zhou, Z. A P2-$Na_{0.67}Co_{0.5}Mn_{0.5}O_2$ Cathode Material with Excellent Rate Capability and Cycling Stability for Sodium Ion Batteries. *J. Mater. Chem. A* **2016**, *4* (28), 11103−11109.

(14) Yan, Z.; Tang, L.; Huang, Y.; Hua, W.; Wang, Y.; Liu, R.; Gu, Q.; Indris, S.; Chou, S.-L.; Huang, Y.; Wu, M.; Dou, S.-X. A Hydrostable Cathode Material Based on the Layered P2@P3 Composite That Shows Redox Behavior for Copper in High-Rate and Long-Cycling Sodium-Ion Batteries. *Angew. Chem.* **2019**, *131* (5), 1426−1430.

(15) Lee, D. H.; Xu, J.; Meng, Y. S. An Advanced Cathode for Na-Ion Batteries with High Rate and Excellent Structural Stability. *Phys. Chem. Chem. Phys.* **2013**, *15* (9), 3304−3312.

(16) Kalapsazova, M.; Ortiz, G. F.; Tirado, J. L.; Dolotko, O.; Zhecheva, E.; Nihtianova, D.; Mihaylov, L.; Stoyanova, R. P3-Type Layered Sodium-Deficient Nickel-Manganese Oxides: A Flexible Structural Matrix for Reversible Sodium and Lithium Intercalation. *ChemPlusChem* **2015**, *80* (11), 1642−1656.

(17) Shi, Y.; Zhang, Z.; Jiang, P.; Gao, A.; Li, K.; Zhang, Q.; Sun, Y.; Lu, X.; Cao, D.; Lu, X. Unlocking the Potential of P3 Structure for Practical Sodium-Ion Batteries by Fabricating Zero Strain Framework for Na^+ Intercalation. *Energy Storage Mater.* **2021**, *37*, 354−362.

(18) Lu, Z.; Dahn, J. R. In Situ X-Ray Diffraction Study of P2-$Na_{2/3}Ni_{1/3}Mn_{2/3}O_2$. *J. Electrochem. Soc.* **2001**, *148* (11), A1225.

(19) Wang, H.; Yang, B.; Liao, X. Z.; Xu, J.; Yang, D.; He, Y. S.; Ma, Z. F. Electrochemical Properties of P2-$Na_{2/3}[Ni_{1/3}Mn_{2/3}]O_2$ Cathode Material for Sodium Ion Batteries When Cycled in Different Voltage Ranges. *Electrochim. Acta* **2013**, *113*, 200−204.

(20) Shi, Y.; Li, S.; Gao, A.; Zheng, J.; Zhang, Q.; Lu, X.; Gu, L.; Cao, D. Probing the Structural Transition Kinetics and Charge Compensation of the P2-$Na_{0.78}Al_{0.05}Ni_{0.33}Mn_{0.60}O_2$ Cathode for Sodium Ion Batteries. *ACS Appl. Mater. Interfaces* **2019**, *11* (27), 24122−24131.

(21) Wang, Y.; Wang, X.; Li, X.; Yu, R.; Chen, M.; Tang, K.; Zhang, X. The Novel P3-Type Layered $Na_{0.65}Mn_{0.75}Ni_{0.25}O_2$ Oxides Doped by Non-Metallic Elements for High Performance Sodium-Ion Batteries. *Chem. Eng. J.* **2019**, *360*, 139−147.

(22) Zhang, L.; Wang, J.; Li, J.; Schuck, G.; Winter, M.; Schumacher, G.; Li, J. Preferential Occupation of Na in P3-Type Layered Cathode Material for Sodium Ion Batteries. *Nano Energy* **2020**, *70*, 104535.

(23) Kubota, K.; Yabuuchi, N.; Yoshida, H.; Dahbi, M.; Komaba, S. Layered Oxides as Positive Electrode Materials for Na-Ion Batteries. *MRS Bull.* **2014**, *39* (5), 416−422.

(24) Gao, R. M.; Zheng, Z. J.; Wang, P. F.; Wang, C. Y.; Ye, H.; Cao, F. F. Recent Advances and Prospects of Layered Transition Metal Oxide Cathodes for Sodium-Ion Batteries. *Energy Storage Mater.* **2020**, *30*, 9−26.

(25) Wang, Q.; Chu, S.; Guo, S. Progress on Multiphase Layered Transition Metal Oxide Cathodes of Sodium Ion Batteries. *Chin. Chem. Lett.* **2020**, *31* (9), 2167−2176.

(26) Jiang, N.; Liu, Q.; Wang, J.; Yang, W.; Ma, W.; Zhang, L.; Peng, Z.; Zhang, Z. Tailoring P2/P3 Biphases of Layered Na_xMnO_2 by Co Substitution for High-Performance Sodium-Ion Battery. *Small* **2021**, *17* (7), 2007103.

(27) Chen, X.; Zhou, X.; Hu, M.; Liang, J.; Wu, D.; Wei, J.; Zhou, Z. Stable Layered P3/P2 $Na_{0.66}Co_{0.5}Mn_{0.5}O_2$ Cathode Materials for Sodium-Ion Batteries. *J. Mater. Chem. A* **2015**, *3* (41), 20708−20714.

(28) Zhou, Y. N.; Wang, P. F.; Niu, Y. B.; Li, Q.; Yu, X.; Yin, Y. X.; Xu, S.; Guo, Y. G. A P2/P3 Composite Layered Cathode for High-Performance Na-Ion Full Batteries. *Nano Energy* **2019**, *55*, 143−150.

(29) Rahman, M. M.; Mao, J.; Kan, W. H.; Sun, C. J.; Li, L.; Zhang, Y.; Avdeev, M.; Du, X. W.; Lin, F. An Ordered P2/P3 Composite Layered Oxide Cathode with Long Cycle Life in Sodium-Ion Batteries. *ACS Mater. Lett.* **2019**, *1* (5), 573−581.

(30) Wang, D.; Chen, H.; Zheng, X.; Qiu, L.; Qu, J.; Wu, Z.; Zhong, Y.; Xiang, W.; Zhong, B.; Guo, X. Simultaneous Component Ratio and Particle Size Optimization for High-Performance and High Tap Density P2/P3 Composite Cathode of Sodium-Ion Batteries. *ChemElectroChem.* **2019**, *6* (19), 5155−5161.

(31) Zheng, J.; Yan, P.; Kan, W. H.; Wang, C.; Manthiram, A. A Spinel-Integrated P2-Type Layered Composite: High-Rate Cathode for Sodium-Ion Batteries. *J. Electrochem. Soc.* **2016**, *163* (3), A584−A591.

(32) Hou, P.; Yin, J.; Lu, X.; Li, J.; Zhao, Y.; Xu, X. A Stable Layered P3/P2 and Spinel Intergrowth Nanocomposite as a Long-Life and High-Rate Cathode for Sodium-Ion Batteries. *Nanoscale* **2018**, *10* (14), 6671−6677.

(33) Zhu, Y.; Xiao, Y.; Hua, W.; Indris, S.; Dou, S.; Guo, Y.; Chou, S. Manipulating Layered P2@P3 Integrated Spinel Structure Evolution for High-Performance Sodium-Ion Batteries. *Angew. Chem.* **2020**, *132* (24), 9385−9390.

(34) Chu, S.; Guo, S.; Zhou, H. Advanced Cobalt-Free Cathode Materials for Sodium-Ion Batteries. *Chem. Soc. Rev.* **2021**, *50* (23), 13189−13235.

(35) Kannan, K.; Kouthaman, M.; Arjunan, P.; Priyanka, V.; Subadevi, R.; Kumaresan, L.; Sivakumar, M. Iron Substituted Layered P2-Type $Na_{1/2}Ti_{6/10}Ni_{3/10}Fe_{1/10}O_2$ as Innovative Anode Material for Rechargeable Sodium Batteries. *Inorg. Chem. Commun.* **2021**, *124*, 108383.

(36) Roisnel, T.; Rodríquez-Carvajal, J. WinPLOTR: A Windows Tool for Powder Diffraction Patterns Analysis T. *Mater. Sci. Forum* **2001**, *378*, 118.

(37) Berar, J. F.; Lelann, P. E.s.d.'s and estimated probable error obtained in Rietveld refinements with local correlations. *J. Appl. Crystallogr.* **1991**, *24* (1), 1−5.

(38) Balachandran, G.; Dixon, D.; Bramnik, N.; Bhaskar, A.; Yavuz, M.; Pfaffmann, L.; Scheiba, F.; Mangold, S.; Ehrenberg, H. Elucidation of the Electrochemical Reaction Mechanism in MFe2O4 (M = Ni, Co) Conversion-Type Negative Electrode Systems by Using In Situ X-Ray Absorption Spectroscopy. *ChemElectroChem* **2015**, *2* (10), 1510−1518.
(39) Liu, H.; Allan, P. K.; Borkiewicz, O. J.; Kurtz, C.; Grey, C. P.; Chapman, K. W.; Chupas, P. J. A Radially Accessible Tubular in Situ X-Ray Cell for Spatially Resolved Operando Scattering and Spectroscopic Studies of Electrochemical Energy Storage Devices. *J. Appl. Crystallogr.* **2016**, *49*, 1665−1673.
(40) Belik, A. A.; Furubayashi, T.; Yusa, H.; Takayama-muromachi, E. Perovskite, $LiNbO_3$, Corundum, and Hexagonal Polymorphs of $(In_{1-x}M_x)$ MO_3. *J. Am. Chem. Soc.* **2011**, *133*, 9405−9412.
(41) Sharma, P.; Das, C.; Indris, S.; Bergfeldt, T.; Mereacre, L.; Knapp, M.; Geckle, U.; Ehrenberg, H.; Darma, M. S. D. Synthesis and Characterization of a Multication Doped Mn Spinel, $LiNi_{0.3}Cu_{0.1}Fe_{0.2}Mn_{1.4}O_4$, as 5 V Positive Electrode Material. *ACS Omega* **2020**, *5* (36), 22861−22873.
(42) Zhang, Z.; Meng, Y.; Wang, Y.; Yuan, H.; Xiao, D. Obtaining P2-$Na_{0.56}[Ni_{0.1}Co_{0.1}Mn_{0.8}]O_2$ Cathode Materials for Sodium-Ion Batteries by Using a Co-Precipitation Method. *ChemElectroChem.* **2018**, *5* (21), 3229−3235.
(43) Yuan, D.; Hu, X.; Qian, J.; Pei, F.; Wu, F.; Mao, R.; Ai, X.; Yang, H.; Cao, Y. P2-Type $Na_{0.67}Mn_{0.65}Fe_{0.2}Ni_{0.15}O_2$ Cathode Material with High-Capacity for Sodium-Ion Battery. *Electrochim. Acta* **2014**, *116*, 300−305.
(44) Zhou, D.; Huang, W.; Zhao, F.; Lv, X. The Effect of Na Content on the Electrochemical Performance of the O3-Type $Na_xFe_{0.5}Mn_{0.5}O_2$ for Sodium-Ion Batteries. *J. Mater. Sci.* **2019**, *54* (9), 7156−7164.
(45) Oh, S. M.; Myung, S. T.; Hwang, J. Y.; Scrosati, B.; Amine, K.; Sun, Y. K. High Capacity O3-Type $Na[Li_{0.05}(Ni_{0.25}Fe_{0.25}Mn_{0.5})_{0.95}]O_2$ Cathode for Sodium Ion Batteries. *Chem. Mater.* **2014**, *26* (21), 6165−6171.
(46) Li, Z. Y.; Gao, R.; Sun, L.; Hu, Z.; Liu, X. Zr-Doped P2-$Na_{0.75}Mn_{0.55}Ni_{0.25}Co_{0.05}Fe_{0.10}Zr_{0.05}O_2$ as High-Rate Performance Cathode Material for Sodium Ion Batteries. *Electrochim. Acta* **2017**, *223*, 92−99.
(47) Peng, H.; Zhang, Y.; Chen, Y.; Zhang, J.; Jiang, H.; Chen, X.; Zhang, Z.; Zeng, Y.; Sa, B.; Wei, Q.; Lin, J.; Guo, H. Reducing Polarization of Lithium-Sulfur Batteries via ZnS/Reduced Graphene Oxide Accelerated Lithium Polysulfide Conversion. *Mater. Today Energy* **2020**, *18*, 100519.
(48) Yuan, D. D.; Wang, Y. X.; Cao, Y. L.; Ai, X. P.; Yang, H. X. Improved Electrochemical Performance of Fe-Substituted Na-$Ni_{0.5}Mn_{0.5}O_2$ Cathode Materials for Sodium-Ion Batteries. *ACS Appl. Mater. Interfaces* **2015**, *7* (16), 8585−8591.
(49) Hasa, I.; Buchholz, D.; Passerini, S.; Scrosati, B.; Hassoun, J. High Performance $Na_{0.5}[Ni_{0.23}Fe_{0.13}Mn_{0.63}]O_2$ Cathode for Sodium-Ion Batteries. *Adv. Energy Mater.* **2014**, *4* (15), 1400083.
(50) Vasilev, G. P.; Pakhomov, L. A.; Ryabova, L. A. Structural and Electrical Properties of DC Sputtered $MnCo_2O_4$ Films. *Thin Solid Films* **1980**, *66* (2), 119−124.
(51) Feltz, A.; Töpfer, J.; Schirrmeister, F. Conductivity Data and Preparation Routes for $NiMn_2O_4$ Thermistor Ceramics. *J. Eur. Ceram. Soc.* **1992**, *9* (3), 187−191.
(52) Xu, S.; Wu, J.; Hu, E.; Li, Q.; Zhang, J.; Wang, Y.; Stavitski, E.; Jiang, L.; Rong, X.; Yu, X.; Yang, W.; Yang, X. Q.; Chen, L.; Hu, Y. S. Suppressing the Voltage Decay of Low-Cost P2-Type Iron-Based Cathode Materials for Sodium-Ion Batteries. *J. Mater. Chem. A* **2018**, *6* (42), 20795−20803.
(53) Han, Y.; Jiang, Y. S.; Yu, F. D.; Deng, L.; Ke, W.; Zhang, S. J.; Que, L. F.; Wu, B.; Ding, F.; Zhao, L.; Wang, Z. B. Addressing Mn Dissolution in High-Voltage $LiNi_{0.5}Mn_{1.5}O_4$ Cathodes via Interface Phase Modulation. *Adv. Funct. Mater.* **2022**, *32* (41), 2207285.
(54) Lin, Y.; Välikangas, J.; Sliz, R.; Molaiyan, P.; Hu, T.; Lassi, U. Optimized Morphology and Tuning the Mn3+ Content of $LiNi_{0.5}Mn_{1.5}O_4$ Cathode Material for Li-Ion Batteries. *Materials (Basel).* **2023**, *16* (8), 3116.
(55) Chen, X.; Song, J.; Li, J.; Zhang, H.; Tang, H. A P2/P3 Composite-Layered Cathode Material with Low-Voltage Decay for Sodium-Ion Batteries. *J. Appl. Electrochem.* **2021**, *51* (4), 619−627.
(56) Ding, F.; Zhao, C.; Zhou, D.; Meng, Q.; Xiao, D.; Zhang, Q.; Niu, Y.; Li, Y.; Rong, X.; Lu, Y.; Chen, L.; Hu, Y. S. A Novel Ni-Rich O3-$Na[Ni_{0.60}Fe_{0.25}Mn_{0.15}]O_2$ Cathode for Na-Ion Batteries. *Energy Storage Mater.* **2020**, *30*, 420−430.
(57) Chen, X.; Li, N.; Kedzie, E.; McCloskey, B. D.; Tang, H.; Tong, W. High-Capacity P2-Type $Na_xLi_{0.25}Mn_{0.75}O_2$ Cathode Enabled by Anionic Oxygen Redox. *J. Electrochem. Soc.* **2019**, *166* (16), A4136−A4140.
(58) Yang, L.; del Amo, J. M. L.; Shadike, Z.; Bak, S. M.; Bonilla, F.; Galceran, M.; Nayak, P. K.; Buchheim, J. R.; Yang, X. Q.; Rojo, T.; Adelhelm, P. A Co- and Ni-Free P2/O3 Biphasic Lithium Stabilized Layered Oxide for Sodium-Ion Batteries and Its Cycling Behavior. *Adv. Funct. Mater.* **2020**, *30* (42), 2003364.
(59) Yabuuchi, N.; Kajiyama, M.; Iwatate, J.; Nishikawa, H.; Hitomi, S.; Okuyama, R.; Usui, R.; Yamada, Y.; Komaba, S. P2-Type $Na_x[Fe_{1/2}Mn_{1/2}]O_2$ Made from Earth-Abundant Elements for Rechargeable NaÂ Batteries. *Nat. Mater.* **2012**, *11* (6), 512−517.
(60) Somerville, J. W.; House, R. A. N.; Tapia-Ruiz, N.; Sobkowiak, A.; Ramos, S.; Chadwick, A. V.; Roberts, M. R.; Maitra, U.; Bruce, P. G. Identification and characterisation of high energy density P2-type $Na_{2/3}[Ni_{1/3-y/2}Mn_{2/3-y/2}Fe_y]O_2$ compounds for Na-ion batteries. *J. Mater. Chem. A* **2018**, *6* (13), 5271−5275.
(61) Yabuuchi, N.; Komaba, S. Recent Research Progress on Iron- and Manganese-Based Positive Electrode Materials for Rechargeable Sodium Batteries. *Sci. Technol. Adv. Mater.* **2014**, *15* (4), 043501.
(62) Boivin, E.; House, R. A.; Marie, J. J.; Bruce, P. G. Controlling Iron Versus Oxygen Redox in the Layered Cathode $Na_{0.67}Fe_{0.5}Mn_{0.5}O_2$: Mitigating Voltage and Capacity Fade by Mg Substitution. *Adv. Energy Mater.* **2022**, *12* (30), 2200702.
(63) Wang, X.; Zhu, M.; Koopal, L. K.; Li, W.; Xu, W.; Liu, F.; Zhang, J.; Liu, Q.; Feng, X.; Sparks, D. L. Effects of Crystallite Size on the Structure and Magnetism of Ferrihydrite. *Environ. Sci. Nano* **2016**, *3* (1), 190−202.
(64) Chu, S.; Zhang, C.; Xu, H.; Guo, S.; Wang, P.; Zhou, H. Pinning Effect Enhanced Structural Stability toward a Zero-Strain Layered Cathode for Sodium-Ion Batteries. *Angew. Chem. Int. Ed.* **2021**, *60* (24), 13366−13371.
(65) Gao, X.; Liu, H.; Deng, W.; Tian, Y.; Zou, G.; Hou, H.; Ji, X. Iron-Based Layered Cathodes for Sodium-Ion Batteries. *Batter. Supercaps* **2021**, *4* (11), 1657−1679.
(66) Xiao, Y.; Zhu, Y. F.; Li, L.; Wang, P. F.; Zhang, W.; Li, C.; Dou, S. X.; Chou, S. L. Structural Insights into the Dynamic and Controlled Multiphase Evolution of Layered-Spinel Heterostructured Sodium Oxide Cathode. *Cell Reports Phys. Sci.* **2021**, *2* (9), 100547.